The Deposition of Bi_2Te_3 and Sb_2Te_3 Thermoelectric Thin-films by Thermal Co-Evaporation and Applications in Energy Harvesting

L.M. Goncalves

University of Minho, Dept. of Industrial Electronics, Azurem, 4800-058 Guimaraes, Portugal
Phone: +351-253510190, Fax: +351-253510189, e-mail: lgoncalves@dei.uminho.pt

Table of contents

1. Introduction

Bismuth, antimony and tellurium compounds (Bi/Sb/Te) are known as the best thermoelectric materials for room temperature operation. Despite thermoelectric devices with these materials being used for many years in macro-scale dimensions (millimetres sized devices), only few attempts were done to reduce these devices to the micro-scale (micrometers sized devices). The deposition of thermoelectric films was reported before using techniques like electrochemical deposition (ECD), metal-organic chemical vapour deposition (MOCVD), pulsed laser deposition (PLD), sputtering and thermal evaporation [1-8]. Each technique has its vantages and disadvantages, and a summary can be found in the table 5.1. In this table, CVD and ECD present opposite characteristics: While CVD films present high figure of merit (ZT), but a low deposition rate and expensive and complicated equipment is required (specific gases are needed for the deposition), ECD is a simple process, allowing high deposition rates (tens of μm can be achieved) but resultant films present low ZT. However, ECD allows the creation of structures during the deposition process, using the LIGA process (from German "Lithographie, Galvanoformung, Abformung", meaning Lithography, Electroplating and Molding). In this chapter, the deposition of Bi_2Te_3 and Sb_2Te_3 thin films by thermal co-evaporation is described.

Table 5.1: Resume of deposition techniques for thermoelectric films.

Technique	**Advantages**	**Disadvantages**
CVD	Very good materials: High ZT.	Low deposition rate. Expensive and complicated equipment.
ECD	Very high deposition rate. Patterning can be done during deposition (LIGA).	Low ZT.
Sputtering	Good deposition rate. Average ZT value. Composition can be controlled with co-sputtering.	Annealing (or substrate heating) improves ZT. Composition difficult to control (depends on power).
Thermal co-evaporation	High ZT. Good deposition rate. Control of film composition. Simple/inexpensive equipment.	Needs substrate heating. Needs precise control of deposition rate and crucible temperature.

The conventional techniques used in the fabrication of macro thermoelectric devices cannot be used in the micro devices. Few pattern techniques have been demonstrated in the fabrication of thermoelectric micro devices, with feature size bellow tens of micrometers. These techniques were imported from the fabrication of MEMS (micro-electro-mechanical systems) techniques, namely wet-etching, lift-off (with SU-8 photoresist), reactive ion etching (RIE) and lithography-electroplating-molding (LIGA). The wet etching patterning process assisted with UV photolithography is presented in this chapter, using thermoelectric Bi/Sb/Te films, in a planar device structure. Applications for micro cooling and energy harvesting are also presented in the end of the chapter.

2. Thin film deposition

The figure of merit of Bi/Sb/Te thermoelectric materials is always related with composition and crystalline structure of materials, despite the technique used. And these properties are related with deposition variables. Previous work [1-3] showed that the optimum composition to maximize the figure of merit is obtained with Te content in the range 60%-65% (atomic). Some of the deposition techniques presented in table 5.1 allow the composition control of the film during growth, thus the figure of merit can be improved. When evaporating directly either Bi_2Te_3, Sb_2Te_3 or $Bi_xSb_{2-x}Te_3$ the materials decompose and the final composition of the film does not match the initial composition of the evaporant, due to the different vapour pressure of the elemental substances Bi, Sb and Te. When heated, these materials decompose, the tellurium evaporates faster than bismuth or antimony, and a composition gradient is expected when thicker films are deposited. The composition differs from the surface layers (Te rich in the first fabricated layers) into the bulk and the last fabricated layers (Bi and Sb rich). A detailed study of composition along thickness was presented by Silva [1]. To overcome this problem, a composition control during film growth is necessary, mainly in thermal evaporation techniques, but also in sputtered films. Using co–evaporation, the deposition rate of each element (Bi, Sb or Te) is controlled independently, and an optimal composition can be achieved [1-4]. The same technique is also used in co-sputtering [5,6].

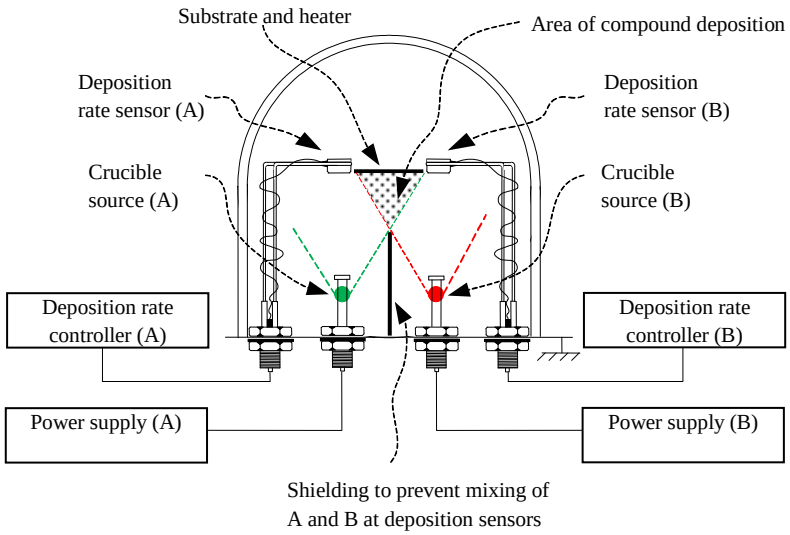

Fig. 5.1: Vacuum chamber prepared for co-evaporation.

A thermal co-evaporation system is presented in fig. 5.1. A pressure bellow 5×10^{-6} is required in a vacuum chamber. The evaporation sources (boats) are in two Molybdenum baffled boxes with volume higher than 4 cm^3. A large volume is required in the boat to maintain deposition properties along the evaporation process, mainly if thick films are pretended. The baffled boxes are used for better stability of deposition rate, compared with typical boats. The power applied to each boat is controlled independently, using a deposition controller (ex: IC6 thin-film deposition controller from Inficon company). The deposition rate of each boat is also measured independently, with a crystal oscillator for each evaporation source. Each crystal sensor is placed carefully in the chamber, in such way that it receives the material evaporated only from the boat it is expected to monitor. A metal sheet is placed between the two boats to partially separate the flows from the two sources, fully preventing mixing of both materials at the quartz crystals (fig. 5.1). The deposition controller [9] computes in real time the power to apply in each boat, using two PID (Proportional Integral and Derivative) algorithms in order to maintain the deposition rate at a fixed value, different for each material. For better results, each deposition monitor should be calibrated considering its position. For this propose, a film should be deposited in the substrate, for each material, and the measured thickness in the monitor corrected to obtain the real thickness of the film (measured with a profilometer or by SEM imaging). A rotating substrate reduces thickness and composition non-uniformity of the films. In the deposition of Bi/Sb/Te films, the substrate should be heated to temperatures (T_{SUB}) in the range between 200 °C and 300 °C. Table 5.2 compares the Seebeck coefficient (α), the resistivity (ρ), the power factor and the figure of merit (ZT) of Bi/Sb/Te films at room temperature (300 K), deposited by different techniques.

Table 5.2: Properties of selected Bi_2Te_3 and $Bi_xSb_{2-x}Te_3$ films

Material and type		***Deposition technique***	***Seebeck α (μVK^{-1})***	***Resistivity ρ (μΩm)***	***Power factor 10^{-3}WK^{-2}m^{-1}***	***ZT @300K***	***Reference***	***Obs***
Bi_2Te_3	n	Co-evaporation	-220	10.6	4.57	0.91	[7]	
Sb_2Te_3	p	Co-evaporation	188	12.6	2.81	0.56	[10]	
Bi_2Te_3	n	Electrochemical	-60	10	0.36	-	[11]	
Bi_2Te_3	n	MOCVD	-210	12	3.7	0.74	[12]	(1)
Sb_2Te_3	p	MOCVD	-110	3.5	3.46	-	[12]	
Bi_2Te_3	p	MOCVD	190	78	0.46	0.75	[13]	(1)
Bi_2Te_3	n	MOCVD	-218	6.9	6.9	-	[14]	
$Bi_{0.5}Sb_{1.5}Te_3$	p	Flash	230	17	3.1	0.87	[15]	
$Bi_2Te_{2.72}Se_{0.3}$	n	Flash	-200	15	2.7	-	[16]	
$Bi_{0.5}Sb_{1.5}Te_3$	p	Flash	240	12	4.8	-	[16]	
$Bi_{1.8}Sb_{0.2}Te_{2.7}Se_{0.3}$	n	Sputtering	-235	47	1.2	-	[17]	(2)
Bi_2Te_3	n	Co-Sputtering	-160	16.3	1.6	-	[6]	(3)
$(BiSb)_2Te_3$	p	Co-Sputtering	175	12.1	2.5	-	[6]	(3)
$Bi_2Se_{0.3}Te_{2.7}$	n	Sputtering	-160	20	1.3	-	[18]	
$Bi_{0.5}Sb_{1.5}Te_3$	p	Sputtering	210	25	1.8	-	[18]	
Bi_2Te_3	n	Co-Sputtering	-55	10	0.3	-	[5]	
Bi_2Te_3	n	Co-evaporation	-228	13.0	4.0	0.81	[19]	(1)
Sb_2Te_3	p	Co-evaporation	171	10.4	2.8	0.53	[19]	(1)
Bi_2Te_3	n	Co-evaporation	-228	28.3	1.8	-	[3]	
Sb_2Te_3	p	Co-evaporation	149	12.5	1.78	-	[3]	

Obs:

(1) Z estimated by the author.

(2) Doped with CuBr.

(3) The power factor of de 3×10^{-3} $WK^{-2}m^{-1}$ and 4×10^{-3} $WK^{-2}m^{-1}$, respectively for type n and type p was reported latter by the same authors [20] but no reference of other thermoelectric properties was found.

Good thermoelectric Bi_2Te_3 films are obtained by co-evaporation, with an evaporation rate of 2 Ås^{-1} at Bi source (Er_{Bi}) and evaporation rate in the range 3-9 Ås^{-1} in the Te source (Er_{Te}). The evaporation flow-rate ratio, $R_{Bi} = Er_{Te} / Er_{Bi}$, is defined as the number of atoms of Te divided by the number of atoms of Bi that arrive in unit time at the substrate during deposition. The power factor is defined as $PF = \alpha^2/\rho$, calculated using the measured Seebeck coefficient (α) and electrical resistivity (ρ). Substrates are heated to the temperature set point in the range between 190 ºC and 270 ºC. All films were deposited in flexible polyimide (Kapton) substrates (fig. 5.2).

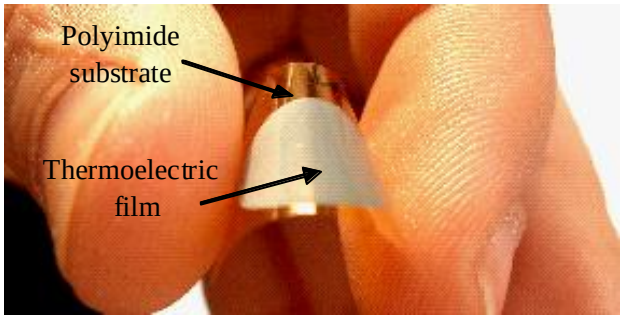

Fig 5.2: Thermoelectric thin film deposited on top of a flexible polyimide (Kapton) substrate [4].

In-plane electrical resistivity, carrier concentration and Hall mobility were measured at room temperature using the conventional four probe van der Pauw geometry in a 5 mm side square arrangement. A DC magnetic field of 80 mT was applied for Hall measurements. The Seebeck coefficient was measured by connecting one side of the film to a heated metal block at a fixed temperature and the other side to a heat sink kept at room temperature, with a temperature difference between both sides below 10 ºC.

The fig. 5.3 compare the thermoelectric properties of 1 µm Bi_2Te_3 films, as function of R_{Bi}, (different evaporation rates of tellurium (Er_{Te}), maintaining the evaporation rate of bismuth Er_{Bi} = 2 $Ås^{-1}$). These properties (Seebeck coefficient, resistivity and carrier concentration) were measured at room temperature, for films deposited with different R_{Bi} and different substrate temperatures (T_{SUB}).

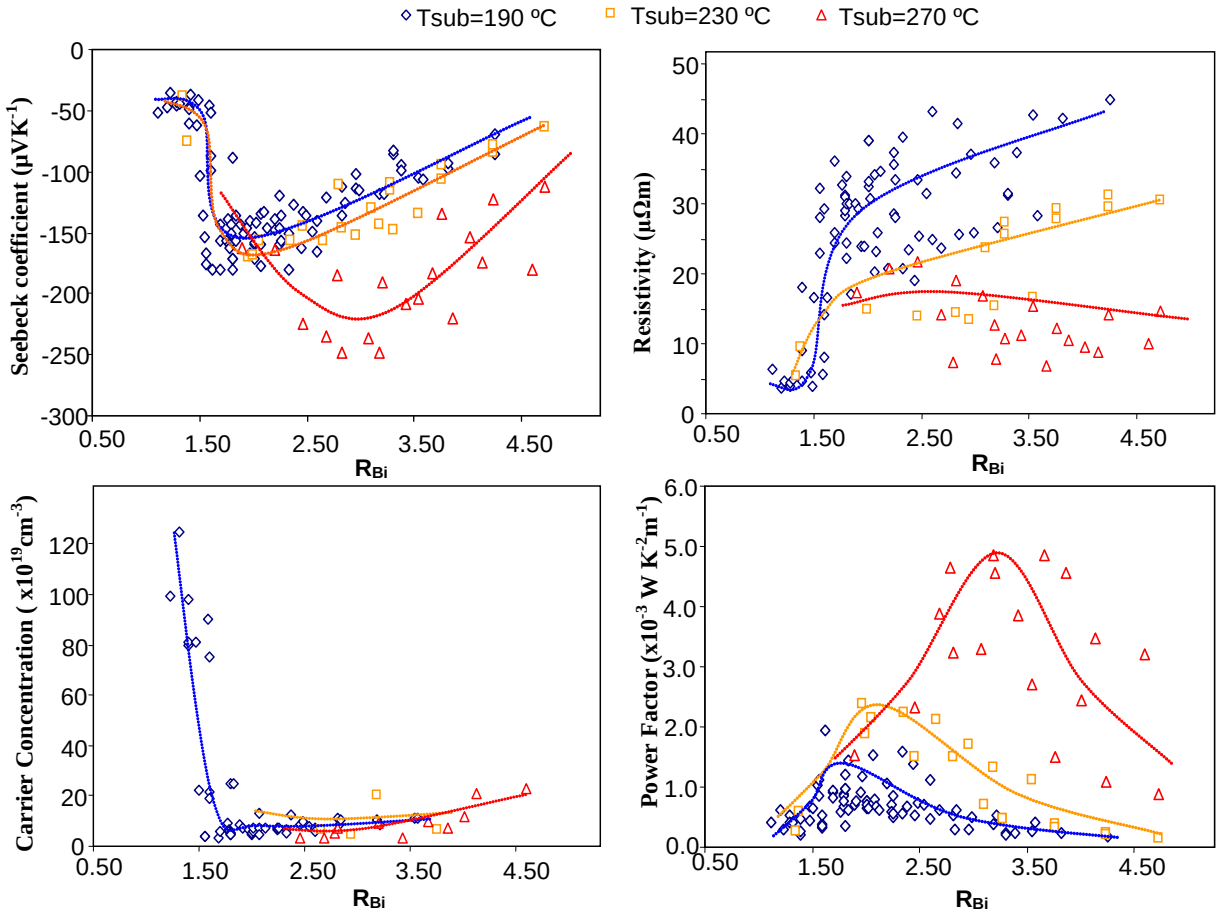

Fig. 5.3: Seebeck coefficient, electrical resistivity, carrier concentration and power factor of Bi_2Te_3 thin films as a function of Te/Bi evaporation flow ratio, R_{Bi} (lines are guides to the eye)[7].

At each T_{sub} the maximum absolute value of the Seebeck coefficient is obtained at a value of R_{Bi} that depends on T_{sub}. Maximum *PF* is obtained at R_{Bi} = 2, 2.5 and 3.5 respectively for T_{sub} = 190, 230 and 270 ºC. Films with compositions in Te richer than stoichiometric have lower carrier concentration (< 10^{20} cm^{-3}), higher mobility (> 50 $cm^2V^{-1}s^{-1}$), and higher Seebeck coefficient, leading to a higher power factor. Films obtained with R_{Bi} < 1.2 are Bi-rich and have high carrier concentration. This results in a decreased value of power factor. High power factor correlates with a high absolute value of Seebeck coefficient, with a low carrier concentration, and with a relatively low electrical resistivity. Since the observed *PF*s dramatically decrease as the carrier concentration and electrical conductivity increase, one is forced to conclude that these increments are the result of major changes in the band structure and position of the Fermi level in the density of states (DOS). These changes are also responsible for the observed decrease in α. In fact, according to the Mott theory of the Seebeck coefficient α, critically depends on the derivative with respect to the energy of the DOS at the Fermi energy [7].

An equivalent behaviour is also found in Sb_2Te3 films. Fig. 5.4 plots the main thermoelectric properties of 1 μm Sb_2Te_3 films, when deposited at different substrate temperatures (T_{SUB} = 150, 180 and 220 ºC) and R_{Sb} in the range 1.4 – 3.7, maintaining the Sb evaporation rate at 2 $Å s^{-1}$.

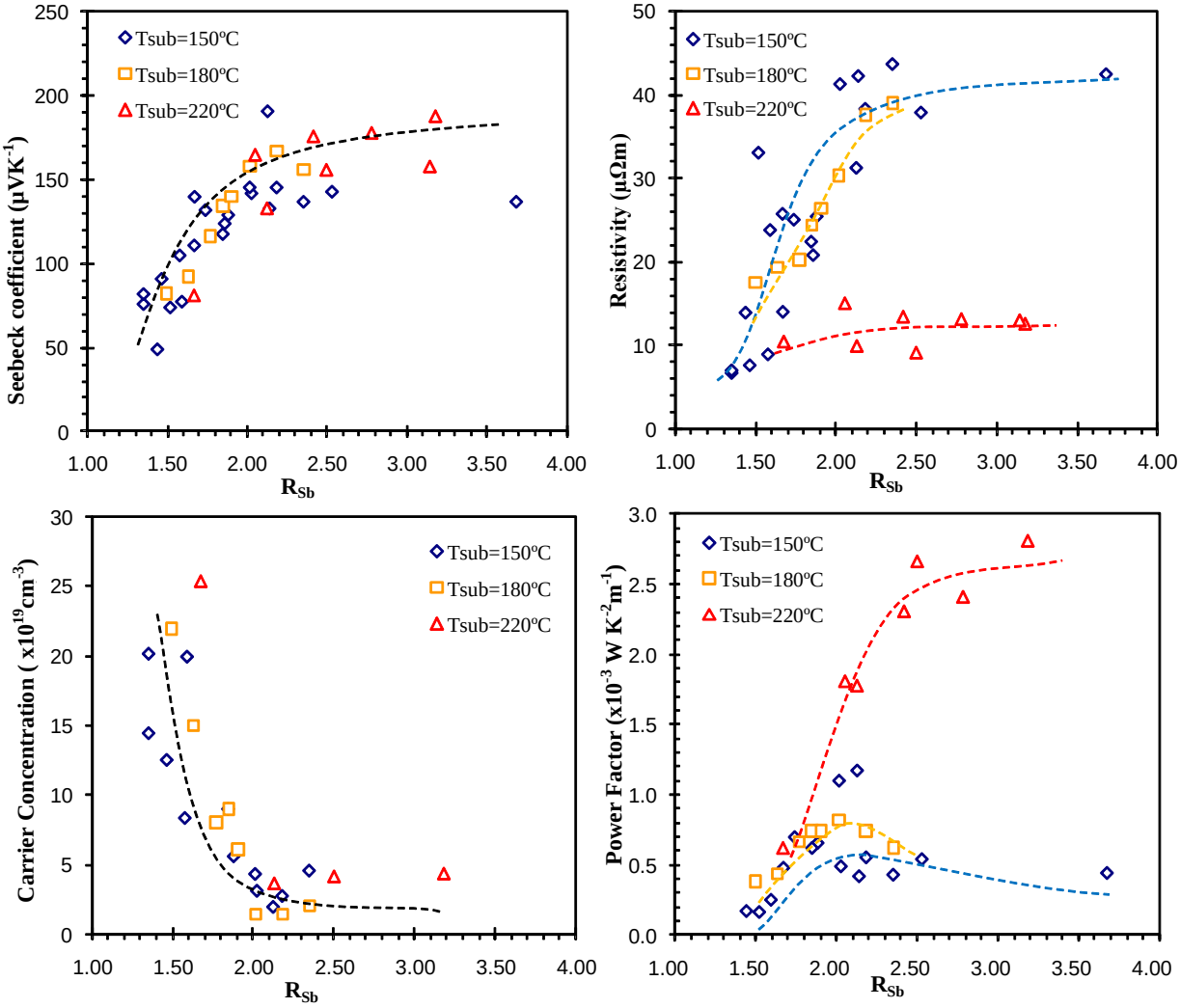

Fig. 5.4: Seebeck coefficient, resistivity, carrier concentration and power factor of Sb_2Te_3 thin-films as a function of Te/Sb evaporation flow ratio, R_{Sb} (lines are guides for the eye). [10]

The value of Seebeck coefficient and the value of electrical resistivity increases as R_{Sb} is increased. The carrier concentration decreases with increase of R_{Sb}. No dependence was found on the Seebeck coefficient or the carrier concentration with the substrate temperature (T_{SUB}). However, the electrical resistivity shows a strong dependence with T_{SUB}. $\rho < 15$ μΩm is obtained with the substrate temperature above 220 ºC. Films with compositions in Te richer than stoichiometric have lower carrier concentration ($n < 5\times10^{19}$ cm^{-3}), higher mobility ($\mu > 100$ $cm^2V^{-1}s^{-1}$), and higher Seebeck coefficient ($\alpha > 150$ μVK^{-1}), leading to a high power factor.

The influence of substrate temperature (T_{SUB}) in the power factor of co-evaporated Bi_2Te_3 and Sb_2Te_3 films [21] is presented in fig. 5.5. The results presented by Zou [2] and Silva [3], also for co-evaporated films, are also presented in the same figure.

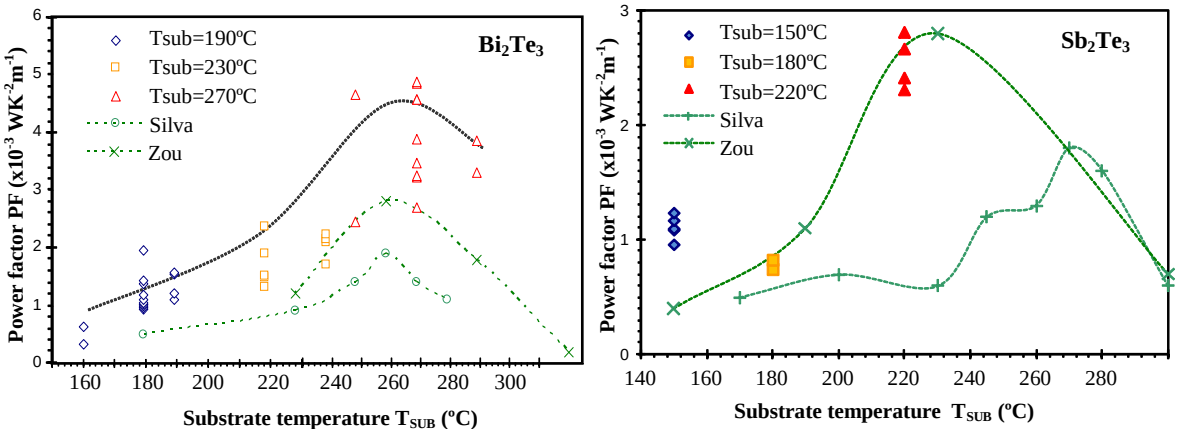

Fig 5.5: Power factor of selected Bi_2Te_3 (left) and Sb_2Te_3 (right) films plotted as a function of substrate temperature T_{SUB} (lines are guides to the eye). Results from Zou [2] and Silva [3] *are also presented.*

The chemical composition of the films and its structure were studied [23] by Energy-Dispersive X-ray spectroscopy. The fig. 5.6 plots the power factor of co-evaporated Bi_2Te_3 and Sb_2Te_3 films, as function of composition (atomic percentage of Te atoms in composition), for films deposited at three different substrate temperatures (T_{SUB}). The power factor of films deposited by Silva [3] using the same deposition technique and the power factor of bulk single crystal of Bi_2Te_3 and Sb_2Te_3 [22] is also presented in the same figure.

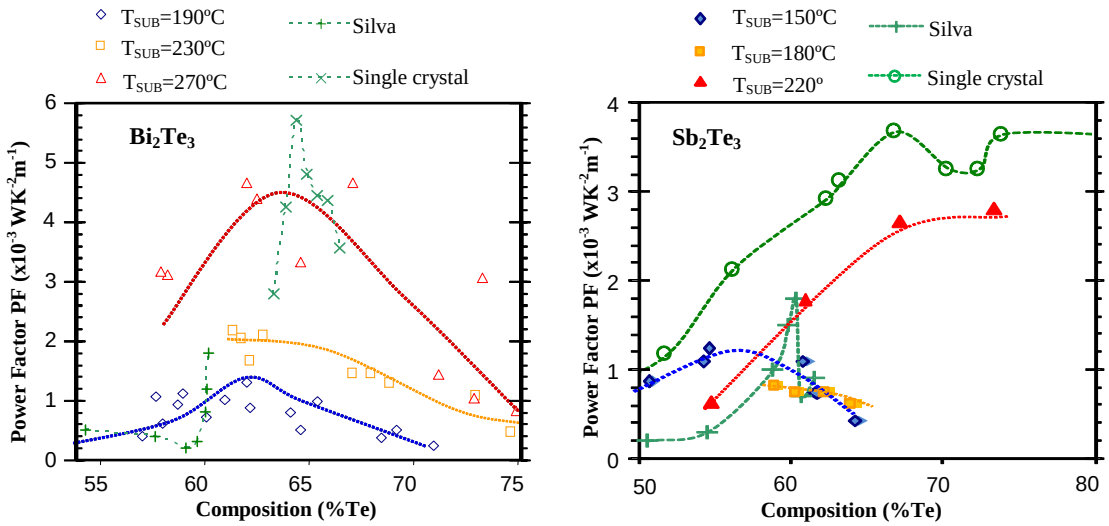

Fig 5.6: Power factor of Bi_2Te_3 (left) and $Sb2_2Te_3$ (right) films deposited by co-evaporation plotted as a function of composition and substrate temperature during deposition (T_{SUB}) (lines are guides to the eye). Results obtained in co-evaporated thin-films from Silva [3] *and from single crystals* [22] *are also presented.*

In the graph of fig. 5.6, Bi_2Te_3 films present the maximum power factor at same composition (aprox. 65% Te) that single crystal Bi_2Te_3. However, the curve along the composition shows a broader peak, probably due to polycrystalline structure of films. The power factor of Sb_2Te_3 films also presents the same behaviour to those of bulk single crystal, when composition varies. The smaller power factor of

Sb_2Te_3 films, compared to bulk is probably due to polycrystalline structure that promotes high electrical resistivity in interface regions.

Thermal conductivity (κ) was measured (in a direction parallel to film) on Bi_2Te_3 films (fig 5.7), for temperatures between -20 ºC and 110 ºC, using the technique described by Völklein [23]. $\kappa = 1.3\ Wm^{-1}K^{-1}$ was obtained at room temperature. Thermal conductivity is due to electron and phonon contributions, respectively κ_e and κ_p, and $\kappa = \kappa_e + \kappa_p$ [24]. Electron contribution was estimated using Wiedemann-Franz law, $\kappa_e = LT/\rho_e$, where L is the Lorenz number, T the temperature and ρ_e is the electrical resistivity. Considering $L = 1.5 \times 10^{-8}\ V^2K^{-2}$ at 300 K [25], $\kappa_e = 0.45\ Wm^{-1}K^{-1}$ is obtained (for a resistivity of 10 μΩm) and $\kappa_p = 0.85\ W\ m^{-1}\ K^{-1}$. This value is smaller than $\kappa_p = 1.03\ Wm^{-1}K^{-1}$ for bulk Bi_2Te_3 [26], due to reduced lattice contribution in polycrystalline structure. Using these values and a Seebeck coefficient of 200 μVK^{-1}, a value of ZT near unity is obtained for the best Bi_2Te_3 thin films at room temperature.

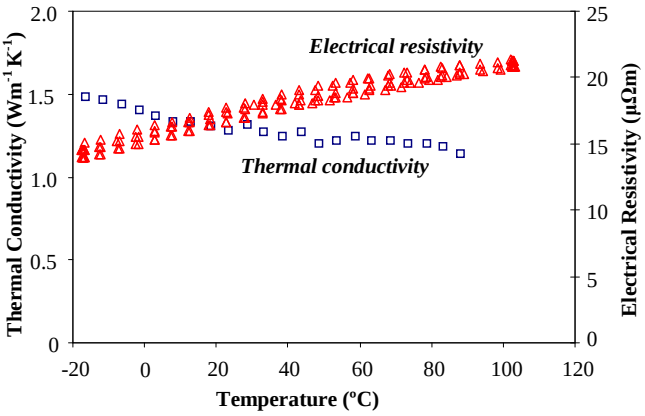

Fig. 5.7: Thermal conductivity and electrical resistivity of a Bi_2Te_3 film, measured from -20 ºC to 110 ºC [7].

Despite de composition, the structure of the thermoelectric thin film is also important to maximize the figure of merit, as demonstrated before [7]. Thermoelectric Bi/Sb/Te films can be amorphous or polycrystalline. Bulk material can also be found in form of single crystal. The interface regions between crystals in a polycrystalline structure create additional electrical resistance, but also reduce thermal conductivity, in such way that films with larger crystal grain have usually a lower resistivity and higher thermal conductivity. The structure of films can be controlled by the substrate temperature during deposition or with post-deposition annealing under controlled atmosphere. Due to decomposition of Bi/Sb/Te compounds with temperature and the low vapour pressure of tellurium (compared with Bi or Sb), this heating process can also alter the composition of films. During deposition (pressure bellow 1×10^{-5} mbar), Te re-evaporates from substrate if temperature exceeds 200 ºC. This can be compensated with a higher evaporation rate of tellurium (beyond stoichiometric composition). A low deposition rate of the films also promotes the growth of crystalline films, and most important in the first film layers (bellow 100 nm). A low growth rate (1 $Ås^{-1}$) in the first 100 nm of film, and increasing up to 6 $Ås^{-1}$, with heated substrate (200 – 300 ºC) achieves higher crystalline structure (and decreases deposition time) than a constant deposition rate of 4 $Ås^{-1}$. In films thicker than 1 μm, deposition rates can either go above 6 $Ås^{-1}$ [21]. Other techniques allow faster growth of films. Böttner [6] reported a deposition rate of 5 μm/h using co-sputtering and Snyder from the JPL laboratory [8] fabricated a device with 20 μm high thermoelectric columns by ECD. Fig. 5.8 and 5.9

shows the difractogram, obtained by X-ray diffraction (XRD) using copper Kα radiation (λ=1.54051Å) of Bi_2Te_3 and Sb_2Te_3 films deposited by co-evaporation, respectively.

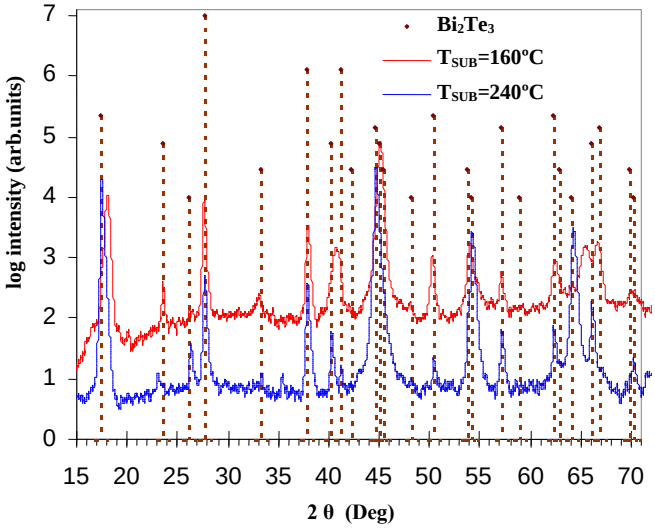

Fig. 5.8: XRD diffractograms of Bi_2Te_3 films deposited at substrate temperatures of 160 ºC (top line) and 240 ºC (bottom line) [7].

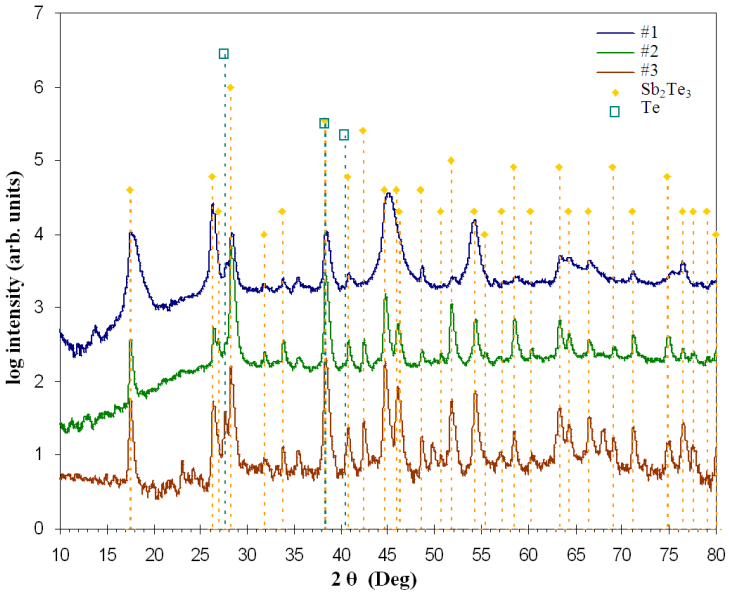

Fig. 5.9: XRD diffractograms of Sb_2Te_3 films.

The observed peaks in fig. 5.8 agree with literature from powder diffraction spectra for polycrystalline Bi_2Te_3, (card 15-863 [27]) or $Bi_{0.43}Te_{0.57}$ (card 22.715 [27]) and are represented in dashed lines. Similar results are also found in literature for the same thermoelectric materials [3,5]. The substrate temperature and the composition influences the peaks found in each film. In Fig 5.8, the two difractograms of Bi_2Te_3 films were obtained with substrate temperatures of T_{SUB} = 160 ºC and T_{SUB} = 240 ºC.

Typical diffractograms of Sb_2Te_3 films are presented in fig. 5.9 from films #1, #2 and #3, respectively deposited at T_{SUB} = 220 ºC, T_{SUB} = 150 ºC and T_{SUB} = 220 ºC and R_{Sb} = 1.7, R_{Sb} = 1.7 and R_{Sb} = 2.5. The planes with the higher X-ray intensities obtained with Sb_2Te_3 films deposited at T_{SUB} = 220 ºC are not the same as those from films deposited at T_{SUB} = 150 ºC or from bulk Sb_2Te_3. The substrate temperature during deposition influences both the structure and the orientation of Sb_2Te_3 thin-films.

Scanning electron microscopy cross-sectional and surface images of films, deposited at optimal (substrate temperature and composition) conditions are presented in fig. 5.10. These images also reveal the polycrystalline structure of film, and grains with dimensions above 500 nm are visible [7,10]. With lower substrate temperature, the dimension of these grains is substantially reduced.

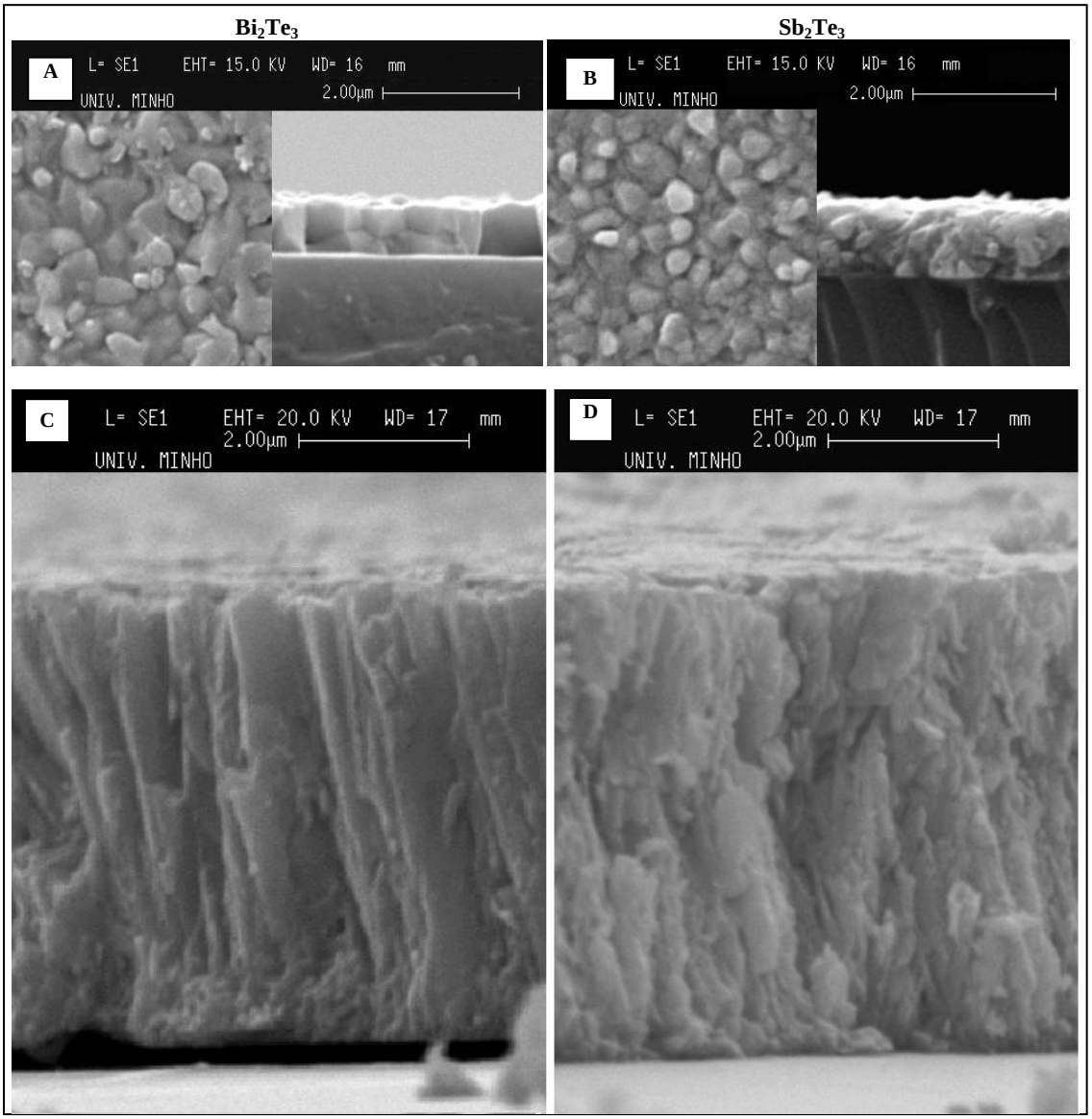

Fig. 5.10: Surface and cross-sectional images of a Bi_2Te_3 films with T_{sub} = 270 ºC and %Te = 62% (A and C) and Sb_2Te_3 films with T_{sub} = 220 ºC and %Te = 70% (B and D), deposited on glass. A and B films have thickness of 1 µm and C and D films have thickness of 5µm. [7,10]

3. Patterning of microdevices

The techniques used in the fabrication of micro thermoelectric devices were imported from the fabrication of MEMS. The must used are wet-etching, lift-off, RIE and LIGA. Micropelt and IPM Freiburg [6] used the RIE technique to pattern thick films of Bi/Sb/Te compounds, using photoresist as an etching mask, using an Oxford-Instruments Bi_2Te_3 ICP etching process [28]. By other way, the JPL laboratory [8] and Institut für Halbleiter und Mikrosystemtechnik [29] fabricated micro-columns of TE materials using a LIGA process, with patterned photoresist and ECD deposition. Lift-off patterning was implemented by the University of Michigan [30-32] . In this technique, thermoelectric films were deposited on top of patterned SU-8 photoresist. The photoresist is then removed, removing also the TE material on top of it, defining the structures. The maximum working temperature of SU-8 photoresist (≈180 ºC) limits the substrate temperature during deposition, thus reducing figure of merit of Bi/Sb/Te films. Shafai [33,34] has reported on the possibility of using nitric acid (HNO_3) and hydrochloric acid (HCl) diluted in water (H_2O) for etching Bi_2Te_3, but that work was not extended to full characterization of the process, and it was not applied to other tellurium compounds. Recent work from Sedky [35] also showed suspended Bi_2Te_3 microstructures fabricated by wet-etching. The use of these etchants in the wet-etching patterning of thermoelectric structures was further studied [4,21,36], using the structures of fig. 5.11. Thermoelectric Bi_2Te_3 and Sb_2Te_3 thin-films (1 µm thick) were deposited on Kapton substrate. Transene's PKP negative photoresist was applied on the surface and test structures were patterned by wet-etching in HNO_3:HCl:H_2O etchant (pure HNO_3 and 37% HCl dil. in water). The effects of etchant composition and dilution in the etch rate are presented in figures 5.12 and 5.13.

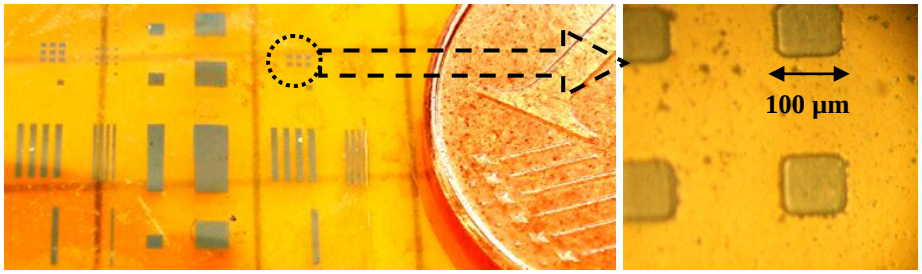

Fig 5.11: Test structures of thermoelectric films patterned by wet-etching.

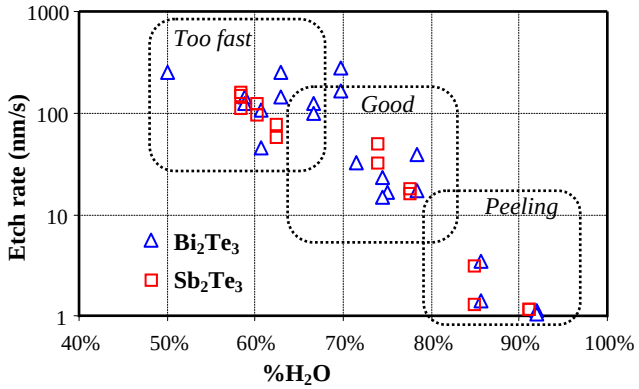

Fig. 5.12: Etch rate of Bi_2Te_3 and Sb_2Te_3 films in 10:3 HNO_3:HCl solution, as a function of dilution in water (% in volume) [36].

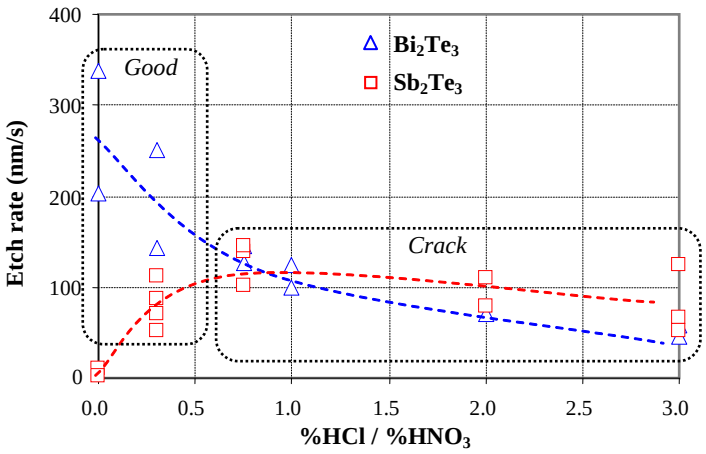

Fig 5.13 Etch rate of Bi_2Te_3 and Sb_2Te_3 films in (1-x)HNO_3:(x)HCl solution (diluted 70% in water, in volume) [36].

The dilution of the etchant (% in volume) in water reduces the etch rate (fig. 5.12). Considering dilutions bellow 70%, the etch rate is to fast (above 100 nm/s) and becomes difficult to accurately control de etch time, occurring frequently over-etching. By the other side, if dilutions above 80% are used, the large time needed for the film in the solution causes peeling of the film. Dilution around 70% is recommended [36]. Figure 5.13 shows the influence of etchant composition on the etch rates. Higher percent of HCl (%HCl / $\%HNO_3$ > 0.5) induces cracking of the film and peeling occurs. Best results are obtained with etchant composition in the range 10:1:20 to 10:5:40 HNO_3:HCl:H_2O. The etch rate of Sb_2Te_3 films in diluted HNO_3 (solution without HCl) was more than 50 times smaller when compared with the etch rate of Bi_2Te_3 films in the same etchant. This is important in terms of the selectivity of the process in the presence of both materials, etching Bi_2Te_3 with HNO_3 while leaving Sb_2Te_3 films untouched. However, this method cannot be used when $Bi_xSb_{2-x}Te_3$ replaces Sb_2Te_3. The etching attack in this solution on $Bi_xSb_{2-x}Te_3$ is similar to that suffered by Bi_2Te_3, even for small values of x.

For chromium and aluminium films using the same etching solutions used for tellurium compounds, etch rates below 0.2 nm/sec were observed regardless of the etchant composition used. Both Bi_2Te_3 and Sb_2Te_3 are slightly etched (<2 nm/s) by aluminium etchant (16:1:1:2 phosphoric acid, nitric acid, acetic acid and water) or Cr etchant (Transene 1020). This selectivity between all films and etchants allows the fabrication of metallic contacts and thermoelectric elements by wet etching. Table 5.3 gathers together all relevant etch rates.

Table 5.3: Summary of etch rates [36].

Material / ***Etchant***	***Bi_2Te_3***	***Sb_2Te_3***	***Aluminium***	***Nickel***
Al – Transene type A	0.8 nm/s	0.5 nm/s	1-8 nm/s	< 0.01 nm/s
Cr - Transene 1020	≈ 2 nm/s	<0.1 nm/s	-	1-4 nm/s
3HNO_3:1HCl (dil 70% H_20)	200 nm/s	80 nm /s	< 0.2 nm/s	< 0.02 nm/s
HNO_3 (dil 70% H_20)	250 nm/s	5 nm/s	< 0.01 nm/s	< 0.01 nm/s

Considering the eatch rates and selectivity presented, the fabrication process of thermoelectric converters of fig. 5.14 can be implemented [36]. P-type Sb_2Te_3 film is first deposited followed by a thin layer (100 nm) of nickel (a).The thin layers of nickel are used to avoid diffusion of thermoelectric

material into the next deposited layers, promoting adhesion and avoiding large contact resistance. Photoresist (PR) is spun and p-type elements are patterned by photolithography (b),(c). Nickel is etched in a chromium etchant (Transene 1020), thermoelectric film is patterned by wet-etching in HNO_3:HCl bath (d) and PR is removed. N-type film is then deposited, followed by a 100 nm nickel layer (e). PR is applied and patterned by photolithography for n-type element definition (f),(g). Nickel is etched in a chromium etchant (Transene 1020), n-type film is etched in HNO_3 (h) and PR removed (i). Contacts are deposited, starting with a 100 nm layer of nickel, followed by 1 μm of aluminium (j). PR is spun and contacts patterned by photolithography (k). Nickel is etched in a chromium etchant (Transene 1020), and aluminium with a standard aluminium etchant (Transene type A). PR is removed (l). A protective layer of Si_3N_4 can also be deposited by low temperature hot-wire chemical vapour deposition (HW-CVD) [37] and patterned if required. Fig 5.15 shows a thermoelectric device fabricated with wet-etching techniques.

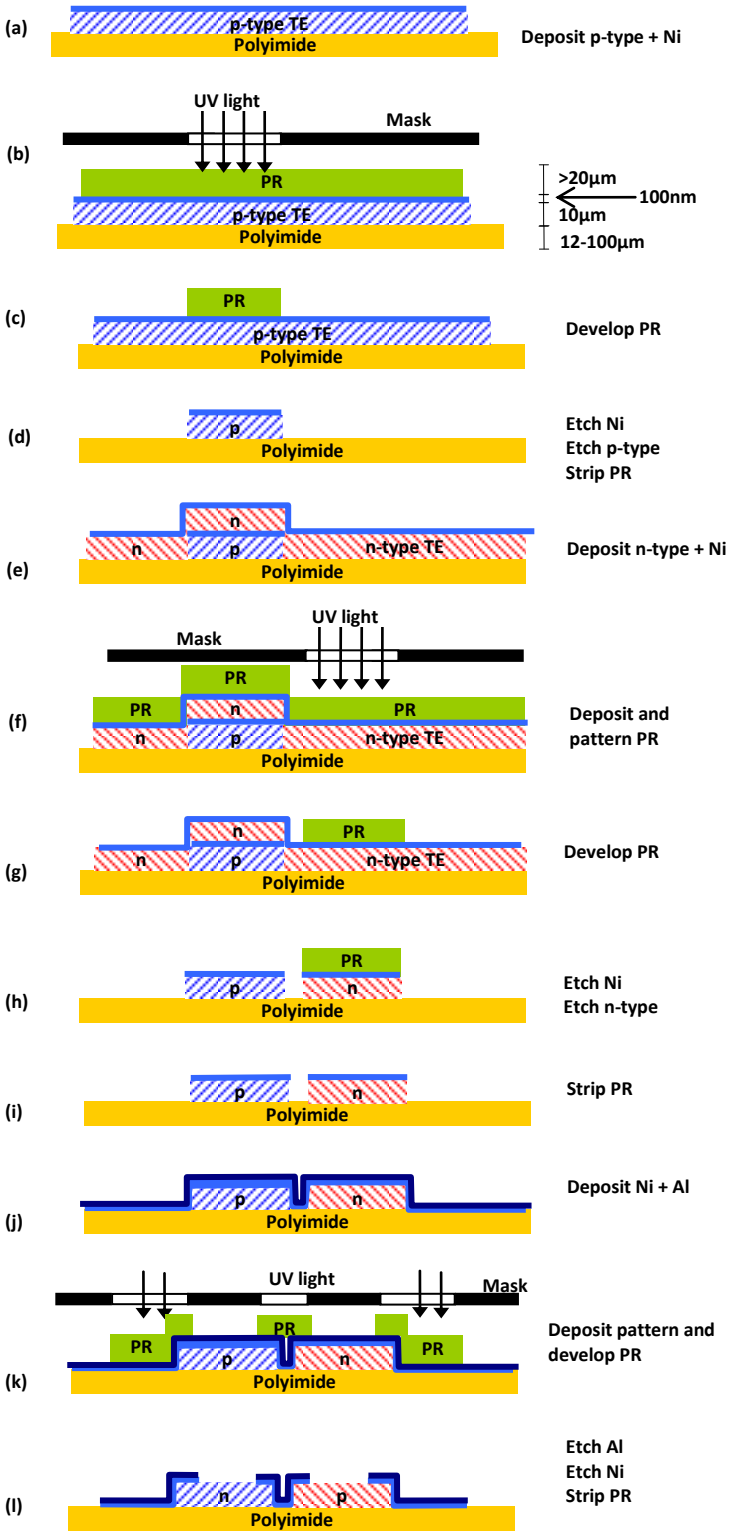

Fig. 5.14: Fabrication steps of thermoelectric converters [36].

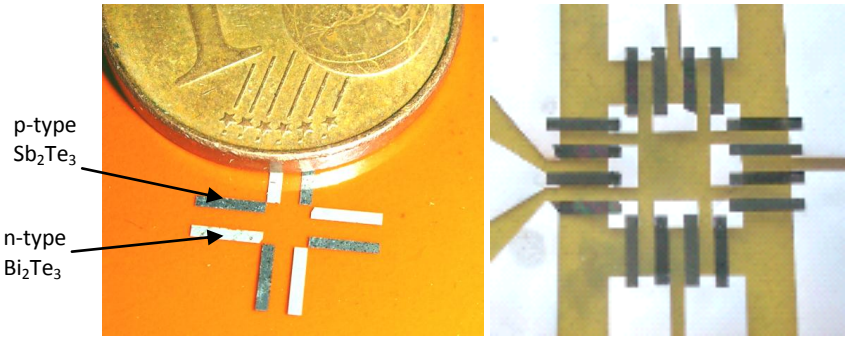

Fig. 5.15: Left: Photo of n-type and p-type elements, before deposition of top contacts. Right: Photo of microcooler with 8 pairs of thermoelectric elements, fabricated with bottom contacts [36].

4. Applications

Using a lateral (in-plane) configuration [38,39], thin-film techniques can be used to scale down the thermoelectric coolers and generators to microdevice dimensions. Planar thin-film technology [4,36] can be used to fabricate such devices. The conventional thermoelectric cooler, with the heat flux perpendicular to hot and cold areas, cannot be scalable to microchip dimensions, using the same fabrication methods used for macro-scale devices. A new design topology [40], a thin-film planar device, as shown in Fig 5.16, has lower heat-pump capacity, but a simplified fabrication process, since all contacts are in the same plane.

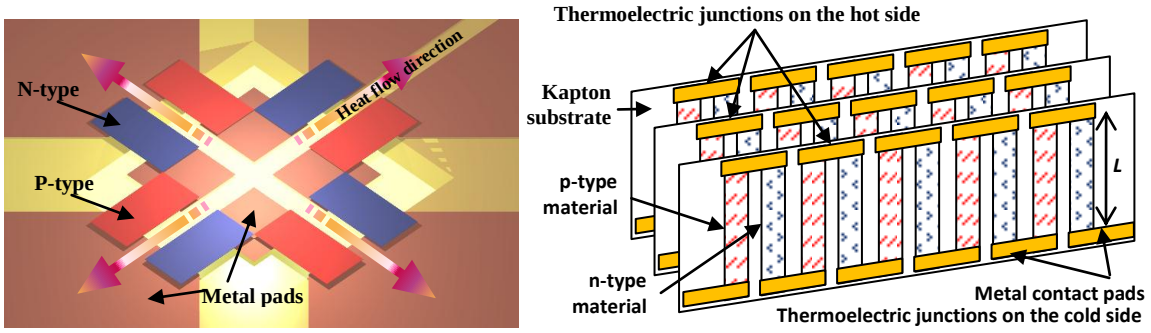

Fig. 5.16: Planar thermoelectric device (left) and array of thermoelectric devices, fabricated in Kapton foils.

Despite using figure of merit to quantify the quality of a thermoelectric material, this parameter can also be used to quantify the performance of a thermoelectric device [40]. The figure of merit of a thermoelectric device is calculated with eq. 1. R_{eq} and K_{eq} are the equivalent electrical resistance and thermal conductance of the device, calculated with eq. 2 and eq. 3.

$$Z = \frac{(\alpha_p - \alpha_n)^2}{K_{eq} R_{eq}} \qquad \text{(Eq. 1)}$$

$$R_{eq} = R_e + 2R_c = \rho_n \frac{L_n}{W_n H_n} + \rho_p \frac{L_p}{W_p H_p} + 2\left(\frac{\rho_{cn}}{L_c W_n} + \frac{\rho_{cp}}{L_c W_p} \right) \qquad \text{(Eq. 2)}$$

$$K_{eq} = \lambda_n \frac{W_n H_n}{L_n} + \lambda_p \frac{W_p H_p}{L_p} + \lambda_m \frac{W_m H_m}{L_m} + 4\gamma W^2 \qquad \text{(Eq. 3)}$$

L_n, L_p, W_n, W_p, H_n, H_p are respectively length, width and height of thermoelectric materials (n-type and p-type) L_c is the length of contacts between TE material and metal pads, α is Seebeck coefficient, ρ electrical resistivity, λ thermal conductivity and ρ_c contact electrical resistivity. The device is supported by an isolating membrane, with thickness H_m, length L_m, width W_m and thermal conductivity λ_m. γ represents a coefficient to include radiation and convection losses, in the range $5 < \gamma < 10$ $Wm^{-2}K^{-1}$.

The previous equations can be used to predict the effect of reducing dimensions of a planar thermoelectric device, from millimetres to micrometers. Besides the Seebeck coefficients (α_n and α_p), the thermal conductivities (λ_n and λ_p) and electrical resistivities (ρ_n and ρ_p) of thermoelectric materials, also the thermal conductivity of the supporting membrane (λ_m) and the contact resistance (ρ_c) influences the performance of planar devices. And the effect of contact resistivity is more pronounced (compared with electrical resistivities) as device dimensions get smaller.

The graph of fig 5.17 presents the effect of scaling down the dimensions of devices, in substrate plane [40]. The scale factor f ″ = 1 (in horizontal axis) represents a device with dimensions L = W = 1 mm, H = 10 µm and H_m = 10 µm. Lower values of f represents devices where dimensions (L and W) were reduced by a factor f, but same thickness (H) considered in thermoelectric materials and membrane.

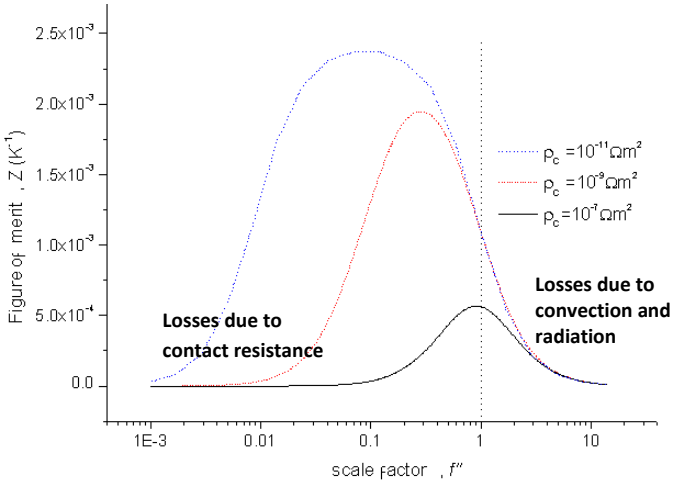

Fig. 5.17: Effect of scaling the device in substrate plane. The height of device and support membrane are constant (H =10 µm and Hm =10µm), while other dimensions are scaled by the value on horizontal axis.

Since the losses by radiation and convection are less relevant in lower dimension devices, figure of merit increases when device is smaller. However, a low contact resistivity must be ensured, to keep this higher figure of merit. Considering both effects, an optimum dimension exists where figure of merit is maximized [40].

4.1. Cooling Applications

A microcooler was fabricated on flexible polyimide Kapton© substrate. The polyimide substrate is excellent for thermoelectric microcoolers in the lateral configuration, because of its small thermal conductivity of 0.15 $Wm^{-1}K^{-1}$ and its thermal expansion coefficient (about 20×10^{-6} K^{-1}) of the same

order of magnitude as that of the thermoelectric films, thus reducing thermal stresses induced during cooling down from the temperature of deposition (200-300 ºC). Fig. 5.15 shows a thermoelectric film deposited on top of a polyimide substrate. Since Bi_2Te_3 and Sb_2Te_3 adhesion is higher on Kapton films than on nickel metal pads, the use of top contacts process (as presented in fig. 5.14) avoids the need of depositing additional layers to promote adhesion of thermoelectric films.

The performance of the microcooler was analysed [41] by use of a thermal image map generated with a microscope equipped with an infrared image sensor. An image [4] under vacuum was obtained with the device excited with a 4 mA current, and cold and hot sides were clearly identified (fig. 5.18). A temperature difference of 5 ºC between the hot and the cold sides was measured under vacuum (10 mtorr) and 4 ºC in still air conditions.

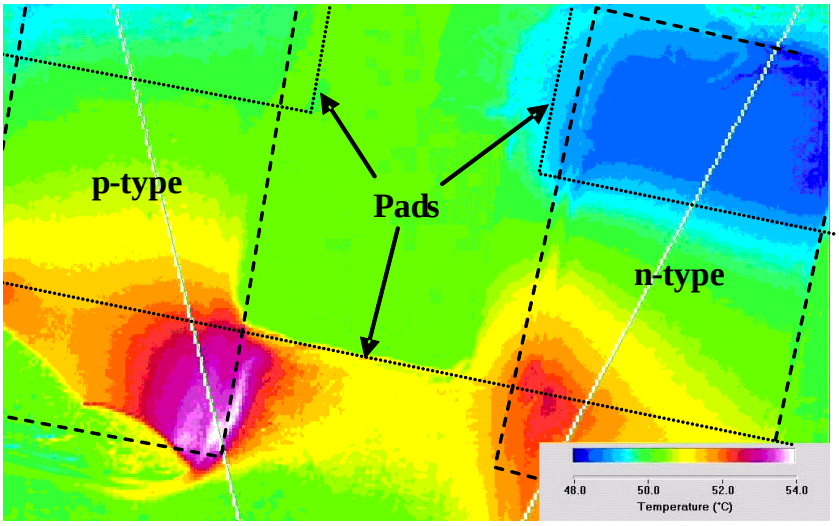

Fig. 5.18: Thermal image of n-type and p-type thermoelectric elements, powered with 4mA current, under vacuum [4].

From the thermal image it is possible to conclude that thermal contact between the thermoelectric elements and the metal pads is poor since the thermal gradient on this region is quite high, compared with the gradient observed along metals or along thermoelectric elements. The 5 ºC hot-cold side temperature difference obtained was lower than the value expected from the simulations. This difference is due to electrical contact resistance, which is much higher than expected. Contact resistance in this device was of the same order of magnitude as the resistance of the thermoelectric elements (2 Ω). A small rectifying barrier voltage (less than 80 μV) was also measured on metal-Bi_2Te_3 contacts.

4.2. Energy Harvesting Applications

This same planar device can be used to implement a thermoelectric generator. Previous work [42-44] has demonstrated the maximum amount of thermal energy that can be removed from human-body in a wearable thermal-generator without compromising the comfort, and maximizing the thermoelectric conversion. A thermal resistance of 100-300 $KW^{-1}cm^2$ is expected in the wrist, where thermal flow can be converted with a thermo-bracelet. Also, temperatures between 27 ºC and 36 ºC can be found on different parts of body. The ambient air temperature and thermal-converter to air thermal resistance also limits the maximum power available. Thermal resistance bellow 50 $KW^{-1}cm^2$ can be achieved with a pin-heatsink. Maximum power output is obtained when the thermal resistance of the thermoelectric generator is equal to the sum of human-body and heat-sink thermal resistances [45,46].

A thermal-resistance above 200 $KW^{-1}cm^2$ is desirable in the thermoelectric converter. Fig. 5.19 shows the open-circuit voltage and maximum power that can be obtained in a 1 cm^2 Bi_2Te_3-Sb_2Te_3 thermoelectric generator, as function of length of the thermoelectric column (length L in fig. 5.16), in a human-body generator, when a temperature difference of 10 ºC (air to body) is available, with 4000 pairs of p-n junctions.

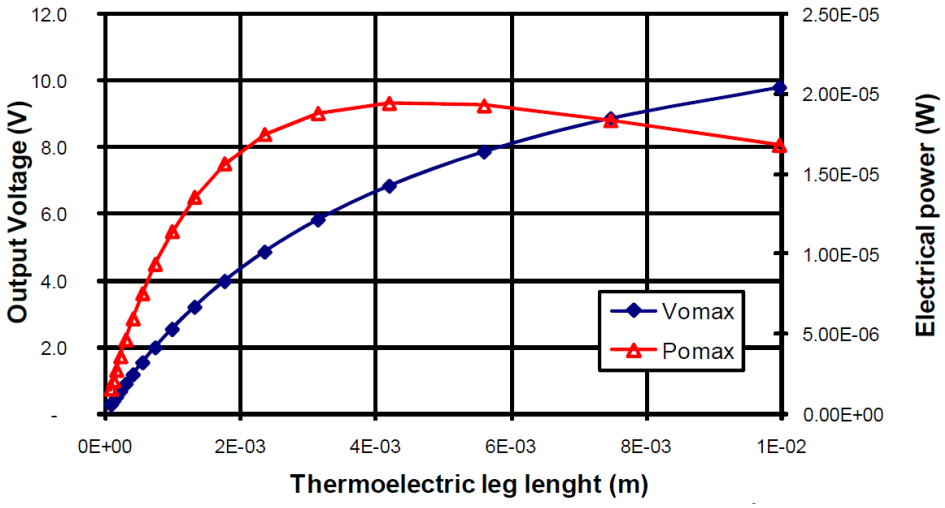

Fig. 5.19: Open-circuit voltage and maximum power that can be obtained in a 1 cm^2 Bi_2Te_3-Sb_2Te_3 thermoelectric generator, as function of length of the column (L), in a human-body generator, when a temperature difference of 10 ºC (air to body) is available.

Since each thermoelectric junction of Bi_2Te_3-Sb_2Te_3 can deliver an output voltage of 300 μVK^{-1}, more than 4000 junctions are necessary to obtain an output voltage (without load) of 10 V, under a temperature difference of 10 ºC, when body and heat-sink thermal resistances are considered. To obtain the desired thermal resistance of 200 $KW^{-1}cm^2$, the thermoelectric elements should have length of about 4 mm. The array of fig 5.16 can be used as a human body energy harvesting device, since many junctions can be stacked in a single device and fabrication process allows the required 4 mm length. Moreover, one of the ribs of fig. 5.16 can contain a solid-state rechargeable battery and another rib the electronic circuit to extract maximum power from the thermoelectric generator and control the charge of the battery [45-48]. Since many of wireless sensors are powered in a peak basis (e.g., the transmission of data needs much more current than standby or receiving mode) and the temperature gradient could not always be present, the energy is stored in a rechargeable thin-film battery of Li-ion type (integrated in the system). Ultra-low power electronics performs DC-DC rectification with a variable conversion factor (using MPPT, maximum power point tracking algorithm) and recharge the battery on optimal conditions. Electronic circuits to perform this task are commercial available [49].

Acknowledgments

The author would like to thank the Portuguese Foundation for Science and Technology (FCT/PTDC/EEA-ENE/66855/2006) for funding this work. Also thank Professor F. Völklein (University of Applied Sciences Wiesbaden) for thermal conductivity measurements, D.M. Rowe and Gao Min (University of Cardiff) for guidelines in this work, P. Alpuim, J.H. Correia, C. Couto, A.G. Rolo, J.P. Carmo, M.F. Silva and J. F. Ribeiro for their help in this work and meaningful discussions.

References

[1] L.W. da Silva and M. Kaviany, “Miniaturized thermoelectric cooler,” *ASME International Mechanical Engineering Congress and Exposition, New Orleans, USA*, 2002, p. 1–15.

[2] H. Zou, D.M. Rowe, and S.G.K. Williams, “Peltier effect in a co-evaporated Sb2Te3(P)-Bi2Te3(N) thin film thermocouple,” *Thin Solid Films*, vol. 408, Apr. 2002, pp. 270-274.

[3] L.W. da Silva, M. Kaviany, and C. Uher, “Thermoelectric performance of films in the bismuth-tellurium and antimony-tellurium systems,” *Journal of Applied Physics*, vol. 97, 2005, p. 114903.

[4] L.M. Goncalves, J.G. Rocha, C. Couto, P. Alpuim, G. Min, D.M. Rowe, and J.H. Correia, “Fabrication of flexible thermoelectric microcoolers using planar thin-film technologies,” *Journal of Micromechanics and Microengineering*, vol. 17, Jul. 2007, p. S168-S173.

[5] D. Kim, E. Byon, G. Lee, and S. Cho, “Effect of deposition temperature on the structural and thermoelectric properties of bismuth telluride thin films grown by co-sputtering,” *Thin Solid Films*, vol. 510, Jul. 2006, pp. 148-153.

[6] H. Bottner, J. Nurnus, a Gavrikov, G. Kuhner, M. Jagle, C. Kunzel, D. Eberhard, G. Plescher, a Schubert, and K.-H. Schlereth, “New Thermoelectric Components Using Microsystem Technologies,” *Journal of Microelectromechanical Systems*, vol. 13, Jun. 2004, pp. 414-420.

[7] L.M. Goncalves, C. Couto, P. Alpuim, A.G. Rolo, F. Volklein, and J.H. Correia, “Optimization of thermoelectric properties on Bi2Te3 thin films deposited by thermal co-evaporation,” *Thin Solid Films*, vol. 518, 2010, p. 2816–2821.

[8] G.J. Snyder, J.R. Lim, C.-K. Huang, and J.-P. Fleurial, “Thermoelectric microdevice fabricated by a MEMS-like electrochemical process.,” *Nature materials*, vol. 2, Aug. 2003, pp. 528-31.

[9] L.M. Goncalves, J. Rocha, J. Correia, and C. Couto, “Control of the Deposition Ratio of Bi2Te3 and Sb2 Te3 in a Vacuum Evaporator for fabrication of Peltier Elements,” *2006 IEEE International Symposium on Industrial Electronics*, Ieee, 2006, pp. 2773-2777.

[10] L.M. Goncalves, P. Alpuim, and A.G. Rolo, J.H. Correia, “Optimization of thermoelectric properties on Sb2Te3 thin films deposited by thermal co-evaporation,” *Thin Solid Films*.

[11] J.R. Lim, G.J. Snyder, C.-K. Huang, J.A. Herman, M.A. Ryan, and J.-P. Fleurial, “Thermoelectric microdevice fabrication process and evaluation at the Jet Propulsion Laboratory (JPL),” *Twenty-First International Conference on Thermoelectrics, 2002. Proceedings ICT ’02.*, 2002, pp. 535-539.

[12] A. Giani, A. Boulouz, F. Pascal-Delannoy, A. Foucaran, E. Charles, and A. Boyer, "Growth of Bi2Te3 and Sb2Te3 thin films by MOCVD," *Materials Science and Engineering: B*, vol. 64, Sep. 1999, pp. 19-24.

[13] A. Giani, F. Pascaldelannoy, A. Boyer, A. Foucaran, M. Gschwind, and P. Ancey, "Elaboration of Bi2Te3 by metal organic chemical vapor deposition," *Thin Solid Films*, vol. 303, Jul. 1997, pp. 1-3.

[14] A. Boulouz, A. Giani, F. Pascal-Delannoy, M. Boulouz, A. Foucaran, and A. Boyer, "Preparation and characterization of MOCVD bismuth telluride thin films," *Journal of Crystal Growth*, vol. 194, Jan. 1998, pp. 336-341.

[15] F. Volklein, "Transport properties of flash-evaporated (Bi1-xSbx)2Te3 films: Optimization of film properties," *Thin Solid Films*, vol. 187, 1990, pp. 253-262.

[16] A. Foucaran, A. Sackda, A. Giani, F. Pascal-Delannoy, and A. Boyer, "Flash evaporated layers of (Bi2Te3–Bi2Se3)(N) and (Bi2Te3–Sb2Te3)(P)," *Materials Science and Engineering B*, vol. 52, Apr. 1998, pp. 154-161.

[17] E. Kessler, A. Ihring, V. Baier, A. Franke, and U. Dillner, "Thin-film infrared thermopile sensors with thermoelectric high-effective materials combination," *Proc. 11th Int. Conference SENSOR, Nurnberg*, 2003, p. 249–254.

[18] M. Stordeur and I. Stark, "Low power thermoelectric generator-self-sufficient energy supply for micro systems," *Thermoelectrics, 1997. Proceedings ICT'97. XVI International Conference on*, IEEE, 1997, p. 575–577.

[19] H. Zou, D.M. Rowe, and G. Min, "Growth of p- and n-type bismuth telluride thin films by co-evaporation," *Journal of Crystal Growth*, vol. 222, Jan. 2001, pp. 82-87.

[20] H. Bottner, J. Nurnus, A. Schubert, and F. Volkert, "New high density micro structured thermogenerators for stand alone sensor systems," *26th International Conference on Thermoelectrics*, IEEE, 2007, pp. 306-309.

[21] L.M. Goncalves, P. Alpuim, and J.H. Correia, "Fabrication of Thermoelectric Devices by Applying Microsystems Technology," *Journal of Electronic Materials*, vol. 39, Jun. 2010, pp. 1516-1521.

[22] H. Scherrer and S. Scherrer, "Bismuth Telluride, Antimony Telluride, and Their Solid Solutions," *CRC handbook of thermoelectrics, edited by D.M. Rowe*, 1987, pp. 211-237.

[23] F. Volklein and T. Starz, "Thermal conductivity of thin films-experimental methods and theoretical interpretation," *Thermoelectrics, 1997. Proceedings ICT'97. XVI International Conference on*, IEEE, 1997, p. 711–718.

[24] C.M. Bhandari, "Minimizing the Thermal Conductivity," *CRC Handbook of thermoelectrics, edited by D.M. Rowe*, CRC Press, 1987, pp. 55-65.

[25] R. Venkatasubramanian, E. Siivola, T. Colpitts, and B. O'Quinn, "Thin-film thermoelectric devices with high room-temperature figures of merit.," *Nature*, vol. 413, Oct. 2001, pp. 597-602.

[26] M. Stordeur, H.T. Langhammer, H. Sobotta, and V. Riede, "Valence Band Structure of (Bi1-xSbx)2Te3 Single Crystals," *Physica Status Solidi (B)*, vol. 104, 1981, p. 513.

[27] Joint Committee on Powder Diffraction Standards, *Powder Diffraction File*, ASTM, Philadelphia, PA, 1967.

[28] http://www.oxford-instruments.com/products/etching-deposition-growth/processes/etch-processes/Pages/bi2te3.aspx, "Oxford Intruments."

[29] W. Qu, M. Ploetner, and W.J. Fischer, "Microfabrication of thermoelectric generators on flexible foil substrates as a power source for autonomous microsystems," *Journal of Micromechanics and Microengineering*, vol. 11, 2001, p. 146.

[30] L.W. da Silva and M. Kaviany, "Fabrication and measured performance of a first-generation microthermoelectric cooler," *Journal of Microelectromechanical Systems*, vol. 14, Oct. 2005, pp. 1110-1117.

[31] B. Huang, C. Lawrence, A. Gross, G.-S. Hwang, N. Ghafouri, S.-W. Lee, H. Kim, C.-P. Li, C. Uher, K. Najafi, and M. Kaviany, "Low-temperature characterization and micropatterning of coevaporated Bi2Te3 and Sb2Te3 films," *Journal of Applied Physics*, vol. 104, 2008, p. 113710.

[32] G.S. Hwang, a J. Gross, H. Kim, S.W. Lee, N. Ghafouri, B.L. Huang, C. Lawrence, C. Uher, K. Najafi, and M. Kaviany, "Micro thermoelectric cooler: Planar multistage," *International Journal of Heat and Mass Transfer*, vol. 52, Mar. 2009, pp. 1843-1852.

[33] C. Shafai and M.J. Brett, "A micro-integrated Peltier heat pump for localized on-chip temperature control," *Proceedings of 1996 Canadian Conference on Electrical and Computer Engineering*, 1996, pp. 88-91.

[34] C. Shafai and M. Brett, "Optimization of BiTe thin films for microintegrated Peltier heat pumps," *Journal of Vacuum Science & Technology A: Vacuum, Surfaces, and Films*, vol. 15, Sep. 1997, p. 2798.

[35] S. Sedky, A. Kamal, M. Yomn, H. Bakr, R. Ghannam, V. Leonov, and P. Fiorini, "Bi2Te3 as an active material for MEMS based devices fabricated at room temperature," *Solid-State Sensors, Actuators and Microsystems Conference, 2009. TRANSDUCERS 2009. International*, IEEE, 2009, p. 1035–1038.

[36] L.M. Goncalves, C. Couto, P. Alpuim, and J.H. Correia, "Thermoelectric micro converters for cooling and energy-scavenging systems," *Journal of Micromechanics and Microengineering*, vol. 18, Jun. 2008, p. 064008.

[37] P. Alpuim, L.M. Goncalves, E. Marins, T. Viseu, S. Ferdov, and J. Bourée, "Deposition of silicon nitride thin films by hot-wire CVD at 100° C and 250° C," *Thin Solid Films*, vol. 517, 2009, p. 3503–3506.

[38] D. Wijngaards, S. Kong, M. Bartek, and R. Wolffenbuttel, “Design and fabrication of on-chip integrated polySiGe and polySi Peltier devices,” *Sensors and Actuators A: Physical*, vol. 85, 2000, p. 316–323.

[39] G. Min and D.M. Rowe, “Cooling performance of integrated thermoelectric microcooler,” *Solid-State Electronics*, vol. 43, May. 1999, pp. 923-929.

[40] L.M. Goncalves, R.P. Rocha, J.P. Carmo, and J.H. Correia, “Solid-state microcoolers and thermal energy harvesting microsystems,” *2009 35th Annual Conference of IEEE Industrial Electronics*, Nov. 2009, pp. 4040-4044.

[41] L.M. Goncalves, J. Rocha, C. Couto, P. Alpuim, and J. Correia, “On-chip array of thermoelectric Peltier microcoolers,” *Sensors and Actuators A: Physical*, vol. 145-146, Jul. 2008, pp. 75-80.

[42] V. Leonov, P. Fiorini, S. Sedky, T. Torfs, and C. Van Hoof, “Thermoelectric mems generators as a power supply for a body area network,” *The 13th International Conference on Solid-State Sensors, Actuators and Microsystems, TRANSDUCERS ’05.*, IEEE, 2005, pp. 291-294.

[43] R.J.M. Vullers, R. van Schaijk, I. Doms, C. Van Hoof, and R. Mertens, “Micropower energy harvesting,” *Solid-State Electronics*, vol. 53, Jul. 2009, pp. 684-693.

[44] V. Leonov and R. Vullers, “Thermoelectric generators on living beings,” *Proceedings of the 5th European Conference on Thermoelectrics (ECT 07)*, 2007, p. 47–52.

[45] J.P. Carmo, R.P. Rocha, A.F. Silva, L.M. Goncalves, and J.H. Correia, “Integrated thin-film rechargeable battery in a thermoelectric scavenging microsystem,” *2009 International Conference on Power Engineering, Energy and Electrical Drives*, Mar. 2009, pp. 359-362.

[46] J.P. Carmo, L.M. Goncalves, and J.H. Correia, “Thermoelectric Microconverter for Energy Harvesting Systems,” *IEEE Transactions on Industrial Electronics*, vol. 57, Mar. 2010, pp. 861-867.

[47] J.P. Carmo, L.M. Goncalves, R.F. Wolffenbuttel, and J.H. Correia, “A planar thermoelectric power generator for integration in wearable microsystems,” *Sensors and Actuators A: Physical*, vol. 161, Jun. 2010, pp. 199-204.

[48] J.P. Carmo, J.F. Ribeiro, M.F. Silva, L.M. Goncalves, and J.H. Correia, “Thermoelectric generator and solid-state battery for stand-alone microsystems,” *Journal of Micromechanics and Microengineering*, vol. 20, Aug. 2010, p. 085033.

[49] http://www.cymbet.com/, “Solid-State Energy Storage for Embedded Energy, Power Back-up and Energy Harvesting.”

List of Figures

Fig. 5.19: Open-circuit voltage and maximum power that can be obtained in a 1 cm^2 Bi_2Te_3-Sb_2Te_3 thermoelectric generator, as function of length of the column (L), in a human-body generator, when a temperature difference of 10 ºC (air to body) is available.

List of Tables